

A Coordinative Control Strategy for Power Electronic Transformer Based Battery Energy Storage Systems

Yuwei Sun^{*}, Jiaomin Liu^{*}, Yonggang Li^{*}, Chao Fu[†], and Yi Wang^{*}

^{*,†}State Key Laboratory of Alternate Electrical Power System with Renewable Energy Sources,
 North China Electric Power University, Baoding, China

Abstract

A power electronic transformer (PET) based on the cascaded H-bridge (CHB) and the isolated bidirectional DC/DC converter (IBDC) is capable of accommodating a large scale battery energy storage system (BESS) in the medium-voltage grid, and is referred to as a power electronic transformer based battery energy storage system (PET-BESS). This paper investigates the PET-BESS and proposes a coordinative control strategy for it. In the proposed method, the CHB controls the power flow and the battery state-of-charge (SOC) balancing, while the IBDC maintains the dc-link voltages with feedforward implementation of the power reference and the switch status of the CHB. State-feedback and linear quadratic Riccati (LQR) methods have been adopted in the CHB to control the grid current, active power and reactive power. A hybrid PWM modulating method is utilized to achieve SOC balancing, where battery SOC sorting is involved. The feedforward path of the power reference and the CHB switch status substantially reduces the dc-link voltage fluctuations under dynamic power variations. The effectiveness of the proposed control has been verified both by simulation and experimental results. The performance of the PET-BESS under bidirectional power flow has been improved, and the battery SOC values have been adjusted to converge.

Key words: Battery energy storage, Coordinative control, LQR, Power electronic transformer, SOC balancing, State-feedback

I. INTRODUCTION

The increasing penetration of intermittent renewable energy resources, such as solar and wind generation, has created more challenges to the planning, operation and stability control of modern power systems [1], [2]. By speedily storing and releasing electrical energy, a battery energy storage system (BESS) adds more flexibility to an original “rigid” system. Thus, the installation of a BESS, especially on a grid scale, is indispensable for suppressing the fluctuations of renewable energy sources and for improving the power quality of the renewable energy involved in power systems [1], [3]-[5].

Normally a PV plant or wind farm with a megawatt (MW) scale is integrated into a medium-voltage (MV) grid [6], and

in China the voltage level is typically 10kV or 35kV, as shown in Fig. 1(a). For a BESS applied in this scenario, a power conversion system (PCS) with high power and MV ratings is crucial. The cascaded H-bridge (CHB) multilevel converter is a practical solution to achieve MV level power conversion, since it can overcome the voltage limits of switching devices and generate multilevel ac waveforms with a low total harmonic distortion (THD) [7]. Many studies have been conducted on single-stage CHB converter based BESSs. Dedicated active-power control of individual converters and state-of-charge (SOC) balancing control of multiple battery units have been reported in [3] and [8], respectively.

However, the adoption of a single-stage CHB in a BESS directly integrates the batteries on the dc buses of the CHB, and engages the problem of voltage-matching. Technically, battery voltage experiences significant variations which are dependent on the SOC and internal impedance voltage drop of the battery [9], [10]. Wide-range voltage variation on dc buses results in a distortion of the multilevel ac output. To ensure a proper grid power transfer, the voltage of a battery

Manuscript received Apr. 24, 2017; accepted Jul. 13, 2017

Recommended for publication by Associate Editor M. Vilathgamuwa.

[†]Corresponding Author: fuchao@ncepu.edu.cn

Tel: +86-0312-7522329, North China Electric Power University

*State Key Laboratory of Alternate Electrical Power System with Renewable Energy Sources, North China Electric Power Univ., China

pack as well as the withstand voltage of the semiconductor switches have to be designed with a certain rating margin [10]. Furthermore, the absence of galvanic isolation makes the safe operation of a BESS more vulnerable. The employment of an intermediary isolated bidirectional DC/DC converter (IBDC) can resolve the preceding issues. As an alternative to a high-power DC/DC converter [11], the IBDC has received a lot of attention as a high-power interface in smartgrids, railway traction [12], etc., due to its attractive features. It provides the functions of galvanic isolation and voltage conversion, and has the advantages of a high power density, bidirectional power transfer capability, ease of realizing soft-switching, a modular and symmetric structure, etc. [13]. Actually, a PCS using a CHB and a IBDC has become more prevalent in the modern power electronic transformer (PET) area, and is expected to play a key role in the active management of distributed energy generation, energy storage systems, and loads [14]-[17]. Therefore, a BESS based on the CHB-IBDC topology is referred to as a PET-BESS in this paper.

Previous studies on CHB-IBDC type PETs in [15]-[17] mainly considered the application of parallel connected IBDCs. In these papers, the CHB controls the sinusoidal grid current. It also controls the summation of the dc-link voltages and voltage balance. Meanwhile, the IBDCs control the parallel output voltage and power balance of each cell. However, for a BESS, the IBDC outputs are connected to split battery units with different control objectives. The sinusoidal ac current and controllable active and reactive power on the grid side, along with the state of charge (SOC) balancing control of the split battery units should be guaranteed. Moreover, to enhance the dynamic feature under bidirectional BESS applications, coordinative control for fast balancing the transient power between the CHB and the IBDC is required. However, few studies have addressed the above control issues. The authors of [18] presented an H bridge and IBDC based BESS, focusing on the circuit optimal design rather than the control strategies for multi-module cascade applications. In [19], coordinative control methods for the CHB and the half-bridge IBDC in the application of a BESS has been reported. This method applies the power feed-forward to the dc-link. However, battery SOC balancing is not taken into account.

This paper presents an overall coordinative control strategy for a PET-BESS. Firstly, the state-feedback and linear quadratic Riccati (LQR) control methods are applied to optimize the CHB controller design. Secondly, a feed-forward path of the active power reference and the switch status of the CHB is added to the dc-link control for the IBDC, which can reduce the dc-link voltage fluctuation under a fluctuating bidirectional power. Thirdly, the battery SOC values are incorporated into the CHB's Hybrid PWM (HPWM) modulation process to achieve the SOC balancing

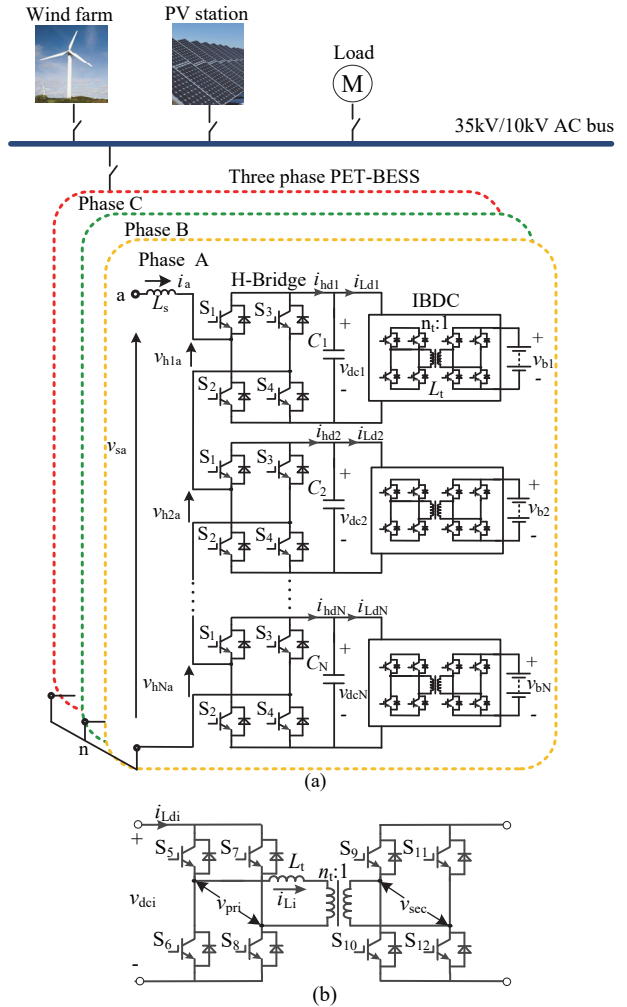


Fig. 1. Main circuit topology of a PET-BESS: (a) entire configuration for a PET-BESS; (b) IBDC circuit composition.

of the submodule battery units.

This paper is organized as follows. Section II briefly introduces the configuration of a PET-BESS and its overall control strategy. Then the designs of the controllers are derived in Section III. Section IV illustrates the HPWM-based SOC balancing method for a CHB rectifier. The proposed control methods are validated by simulation and experimental results in Section V, and some conclusions are given in Section VI.

II. SYSTEM CONFIGURATION

A. Topology and Modeling of a PET-BESS

Fig. 1(a) shows the configuration of a PET-BESS, which consists of a CHB rectifier, N dc-link capacitors $C_1 \sim C_N$, and N IBDC circuits per phase. The components in the leg of phase A are depicted in detail. v_{sa} and i_a are the grid voltage and grid current, respectively; L_s is the input filter inductance; $v_{h1a} \sim v_{hNa}$ are the ac output voltages of each H-bridge of the CHB; $v_{dc1} \sim v_{dcN}$ are the dc-link voltages; $i_{hd1} \sim i_{hdN}$ and $i_{ld1} \sim i_{ldN}$ are the dc

currents before and after the dc-link capacitor, respectively; and $v_{b1} \sim v_{bN}$ are the battery-unit terminal voltages. The circuit composition of the IBDC module is shown in Fig. 1(b), where n_t and L_t are the turn ratio and equivalent leakage inductance (on primary side) of the HF transformer, respectively; i_{Li} is the ac current flowing into the HF transformer; and v_{pri} and v_{sec} are the ac voltages of the primary side and secondary side of the transformer.

Since the objectives of the balancing control in this paper are the dc-link voltages and battery-SOC values among the submodules within one phase leg, the following assumptions are made: 1) the three-phase grid voltages are balanced; 2) the three phase legs have equal average dc-link voltages and average battery SOC values; 3) the converter parameters of each module in each phase are identical.

Since the same IBDC controllers and SOC balancing algorithm are applied to all of the phases, the dc variables on the dc-link and battery side are not distinguished with subscripts a, b and c.

According to Fig. 1, assuming that the dc-link voltages are effectively controlled to the desired reference value v_{dcref} , i.e., $v_{dc1} = v_{dc2} = \dots = v_{dcN} = v_{dcref}$, the relationship between the input quantities and the output quantities of the CHB converter in phase A can be written as follows:

$$\begin{cases} v_{an} = \sum_{i=1}^N v_{bia} = \sum_{i=1}^N h_{ia} \cdot v_{dc1} = v_{dcref} \sum_{i=1}^N h_{ia} \\ i_{hd1} = h_{ia} i_a, \quad (i=1, 2 \dots N) \end{cases} \quad (1)$$

where v_{an} is the synthesized multilevel ac voltage of the CHB, and h_{ia} ($i=1 \dots N$) represents the switching function of each H-bridge. When the two upper switches (S_1, S_3) or the two bottom switches (S_2, S_4) conduct, h_{ia} is equal to zero; when the diagonal switches (S_1, S_4) or (S_2, S_3) conduct, h_{ia} is equal to 1 or -1, respectively. Then based on the KVL, the grid current dynamic is expressed by the following equation:

$$L_s \frac{di_a}{dt} + R_s i_a = v_{sa} - v_{an} = v_{sa} - v_{dcref} \sum_{i=1}^N h_{ia} \quad (2)$$

The ac current dynamic equation of the CHB in the three-phase frame is expressed as:

$$\frac{d}{dt} [i]_{abc} = -\frac{R_s}{L_s} [i]_{abc} - \frac{v_{dcref}}{L_s} [u]_{abc} + \frac{1}{L_s} [v_s]_{abc} \quad (3)$$

where $[v_s]_{abc}$ denotes the grid phase-voltage vector $[v_{sa} \ v_{sb} \ v_{sc}]^T$; $[i]_{abc}$ denotes the grid current vector $[i_a \ i_b \ i_c]^T$, and $[u]_{abc}$ represents the control input vector $[\sum h_{ia} \ \sum h_{ib} \ \sum h_{ic}]^T$ ($i=1 \dots N$).

The park transform is as follows:

$$T_{abc/dq0} = \frac{2}{3} \begin{pmatrix} \cos \omega t & \cos(\omega t - 120^\circ) & \cos(\omega t + 120^\circ) \\ \sin \omega t & \sin(\omega t - 120^\circ) & \sin(\omega t + 120^\circ) \\ 0.5 & 0.5 & 0.5 \end{pmatrix} \quad (4)$$

Applying a park transform to Equation (3), a two-phase rotating frame d - q model of the CHB is obtained as:

$$\begin{cases} \frac{di_d}{dt} = -\frac{R_s}{L_s} i_d + \omega i_q + \frac{v_{sd}}{L_s} - \frac{v_{dcf}}{L_s} \sum_{i=1}^N h_{id} \\ \frac{di_q}{dt} = -\omega i_d - \frac{R_s}{L_s} i_q + \frac{v_{sq}}{L_s} - \frac{v_{dcf}}{L_s} \sum_{i=1}^N h_{iq} \end{cases} \quad (5)$$

where v_{sd} , v_{sq} , i_d , i_q , $\sum h_{id}$ and $\sum h_{iq}$ are the ac voltages, grid currents, and control input signals in the synchronously rotating d - q coordinates, respectively; and $v_{sq}=0$ under the proper synchronization of the space-vector transformation.

The dc-link voltage is determined by the difference between the output dc current i_{hd1} of the H-bridge rectifier and the input dc current i_{Ldi} of the IBDC, as is given by:

$$\begin{cases} i_{Ldi} = \frac{n_t v_{bi}}{2 f_s L_t} D_i (1 - |D_i|) \\ C_i \frac{dv_{dei}}{dt} = i_{hd1} - i_{Ldi} = h_{ia} i_a - \frac{n_t v_{bi}}{2 f_s L_t} D_i (1 - |D_i|) \end{cases} \quad (6)$$

where D_i and f_s represent the phase shift ratio and switching frequency of the IBDC, respectively [11]. According to (6), the dc-link voltage control can be realized by both the outer loop of the grid current controller of the CHB and the direct phase shift regulation of the IBDC. Since the battery voltages change very slowly in contrast to the other variables such as the dc-link voltages and grid currents, the IBDC output voltage v_{bi} can be regarded as a constant and does not need to be controlled. Thus, the IBDC is used to regulate the dc-link in this paper by directly adjusting the phase shift ratio.

B. Overall Coordinative Control Strategy for a PET-BESS

According to the above mathematic analysis, the overall coordinative control system of a PET-BESS, as depicted in Fig. 2, includes three parts: 1) the total active and reactive power control for the three-phase star-configured CHB rectifier based on the state feedback method in the d - q coordinates; 2) the dc-link voltage control on the IBDC by the phase shift ratio with feedforward of the power reference and switch status (switch functions) of the CHB; 3) the HPWM multilevel modulation for the CHB, which aims at balancing control of the submodule battery SOC values, $SOC_1 \sim SOC_N$.

In practical applications, there are some other concerns which should be considered, such as the power limit of the battery units and power variation rate of the BESS, which are determined by the Battery Energy Management System (BEMS) [1] and are not discussed in this paper.

III. PRINCIPLE AND DESIGNING OF THE CONTROLLERS

A. State-Feedback Optimal Control for the CHB Rectifier

By defining the state vector $x=(i_d \ i_q)^T$ and control input vector $u=(\sum h_{id} \ \sum h_{iq})^T$, Equation (5) can be grouped into the following MIMO affine linear form [20]:

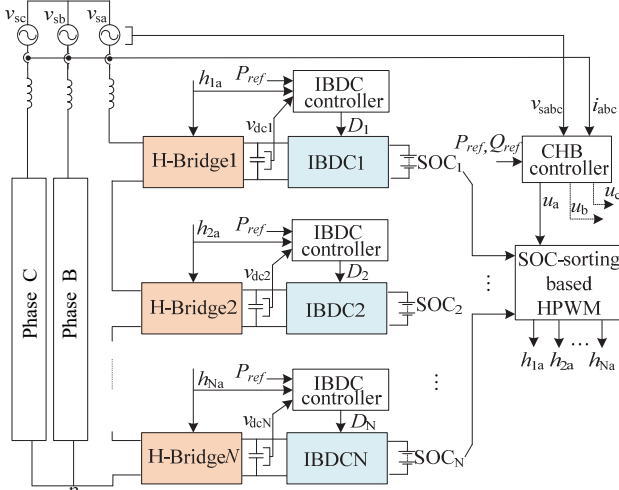


Fig. 2. Block diagram of the proposed overall coordinative control strategy for a PET-BESS.

$$\begin{cases} \dot{\mathbf{x}} = \mathbf{M}\mathbf{x} + \mathbf{b} + \mathbf{Nu} \\ \mathbf{y} = \mathbf{x} - \mathbf{d} \end{cases} \quad (7)$$

$$\mathbf{M} = \begin{pmatrix} -\frac{R_s}{L_s} & \omega \\ -\omega & -\frac{R_s}{L_s} \end{pmatrix}, \mathbf{b} = \begin{pmatrix} +\frac{v_{sd}}{L_s} \\ 0 \end{pmatrix}, \quad (8)$$

$$\mathbf{N} = -\frac{v_{dcref}}{L_s} \begin{pmatrix} 1 & 0 \\ 0 & 1 \end{pmatrix}, \mathbf{d} = \begin{pmatrix} i_{dref} \\ i_{qref} \end{pmatrix}$$

By observing its structure, Equation (7) can be identified as the affine linear form for N is a constant matrix; \mathbf{M} denotes the coefficient matrix, while \mathbf{b} and \mathbf{d} denotes the affine items.

Then, the original affine control system can be easily transformed into a Brunovsky normalized linear form, as demonstrated in (9). This is done through the state-feedback control law illustrated in (10).

$$\begin{cases} \dot{\mathbf{z}} = \mathbf{Az} + \mathbf{Bv} \\ \mathbf{y} = \mathbf{z} \end{cases}, \mathbf{A} = \begin{pmatrix} 0 & 0 \\ 0 & 0 \end{pmatrix}, \mathbf{B} = \begin{pmatrix} 1 & 0 \\ 0 & 1 \end{pmatrix} \quad (9)$$

$$\mathbf{u} = -\mathbf{N}^{-1}(\mathbf{M}\mathbf{x} + \mathbf{b} - \mathbf{v}) = \begin{pmatrix} u_1 \\ u_2 \end{pmatrix} = \frac{1}{v_{dcref}} \begin{pmatrix} -R_s i_d + L_s \omega i_q + v_{sd} - L_s v_1 \\ -L_s \omega i_d - R_s i_q - L_s v_2 \end{pmatrix} \quad (10)$$

where $\mathbf{z} = \mathbf{x} - \mathbf{d}$ denotes the new state variable, and $\mathbf{v} = (v_1 \ v_2)^T$ denotes the new control variable vector.

Since \mathbf{v} is the control variable of the Brunovsky normalized form, it can be determined by the LQR method [21]. Note that system (9) is easier to handle since matrix \mathbf{A} and \mathbf{B} are trivial. According to the LQR method, the quadratic performance index is defined in Equation (11):

$$J = \frac{1}{2} \int_0^\infty (\mathbf{z}^T \mathbf{Q} \mathbf{z} + \mathbf{v}^T \mathbf{R} \mathbf{v}) dt \quad (11)$$

where \mathbf{Q} is a positive definite (or semi-definite) symmetric matrix, and \mathbf{R} is a positive definite symmetric matrix. The

physical meanings of the performance index are explained as follows: the first item indicates that the state error is close to zero during the control process, and the second item aims to restrict the amplitudes of the control variables.

Based on the LQR method, the optimal control law is expressed as follows:

$$\mathbf{v}^* = -\mathbf{K}^* \mathbf{z}(t) = -\mathbf{K}^* \begin{pmatrix} i_d - i_{dref} \\ i_q - i_{qref} \end{pmatrix} \quad (12)$$

where the gain matrix is $\mathbf{K}^* = \mathbf{R}^{-1} \mathbf{B}^T \mathbf{P}$, and \mathbf{P} is the positive definite symmetric solution of the Riccati equation $\mathbf{P} \mathbf{A} + \mathbf{A}^T \mathbf{P} - \mathbf{P} \mathbf{B} \mathbf{R}^{-1} \mathbf{B}^T \mathbf{P} + \mathbf{Q} = \mathbf{0}$, which can be simplified to $-\mathbf{P} \mathbf{R}^{-1} \mathbf{P} + \mathbf{Q} = \mathbf{0}$ in this case.

However, due to the dependence of the affine linear transformation on the parameters of the system and converter, as shown in (10), the zero steady-state error when subjected to temperature or aging parameter variations cannot be ensured by using the simple proportional feedback control law of (12). To solve this problem, an integral term is introduced to the state variable vector, as is given by:

$$\mathbf{z} = (\xi_1 \ z_1 \ \xi_2 \ z_2)^T. \quad (13)$$

where $\xi_1 = \int z_1 dt$, $\xi_2 = \int z_2 dt$.

Substituting (13) in to (9) and (12) yields an expanded linear normal form of the CHB system, as shown in (14), where its new feedback control law is shown in (15).

$$\begin{cases} \dot{\mathbf{z}} = \mathbf{Az} + \mathbf{Bv} \\ \mathbf{y} = \mathbf{z} \end{cases} \quad (14)$$

$$\mathbf{A} = \begin{pmatrix} 0 & 1 & 0 & 0 \\ 0 & 0 & 0 & 0 \\ 0 & 0 & 0 & 1 \\ 0 & 0 & 0 & 0 \end{pmatrix}, \mathbf{B} = \begin{pmatrix} 0 & 0 \\ 1 & 0 \\ 0 & 0 \\ 0 & 1 \end{pmatrix}, \mathbf{v} = \begin{pmatrix} v_1 \\ v_2 \end{pmatrix}$$

$$\begin{pmatrix} v_1 \\ v_2 \end{pmatrix} = -\mathbf{K}^* (\xi_1 \ z_1 \ \xi_2 \ z_2)^T$$

$$= -\begin{pmatrix} k_1 & k_2 & 0 & 0 \\ 0 & 0 & k_3 & k_4 \end{pmatrix} \begin{pmatrix} \int (i_d - i_{dref}) dt \\ i_d - i_{dref} \\ \int (i_q - i_{qref}) dt \\ i_q - i_{qref} \end{pmatrix} \quad (15)$$

With the integral term added to the linear feedback control law, as shown in (15), the zero steady-state error and robustness of the CHB controller can be enhanced.

To solve the feedback gain matrix \mathbf{K}^* through the LQR method, the weight matrix \mathbf{Q} and \mathbf{R} of the quadratic performance index shown in (11) must be determined first. For matrix \mathbf{Q} , the system energy function is constructed as:

$$H = \mathbf{z}^T \mathbf{Q} \mathbf{z} = \frac{L_s}{2} (\xi_1^2 + z_1^2 + \xi_2^2 + z_2^2) \quad (16)$$

By substituting $\mathbf{z} = (\xi_1 \ z_1 \ \xi_2 \ z_1)^T$ into (16), the matrix \mathbf{Q} can be determined as:

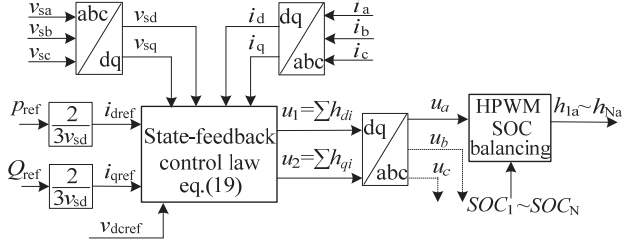


Fig. 3. Block diagram of the CHB control.

$$\mathbf{Q} = \frac{L_s}{2} \begin{pmatrix} 1 & 0 & 0 & 0 \\ 0 & 1 & 0 & 0 \\ 0 & 0 & 1 & 0 \\ 0 & 0 & 0 & 1 \end{pmatrix} \quad (17)$$

Another weighted matrix \mathbf{R} is selected as:

$$\mathbf{R} = \frac{L_s^2}{f_c} \begin{pmatrix} 1 & 0 \\ 0 & 1 \end{pmatrix} \quad (18)$$

where f_c is the equivalent switching frequency of the CHB rectifier. It can be seen that \mathbf{Q} is indeed a positive semi-definite and that \mathbf{R} is indeed a positive definite.

Then by substituting \mathbf{A} , \mathbf{B} , \mathbf{Q} and \mathbf{R} shown in (14), (17) and (18) into the Riccati equation, the matrix \mathbf{P} and matrix \mathbf{K}^* can be determined. Substituting the matrix \mathbf{K}^* into (15) and (10) yields the control vector \mathbf{u} for the original system, which is shown as follows:

$$\begin{cases} u_1 = \frac{L_s \omega i_q - R_s i_d + v_{sd} + L_s (k_1 \xi_1 + k_2 z_1)}{v_{dcref}} \\ u_2 = \frac{-L_s \omega i_d - R_s i_q + L_s (k_3 \xi_2 + k_4 z_2)}{v_{dcref}} \end{cases} \quad (19)$$

Based on (19), a control block diagram of the CHB rectifier is shown in Fig. 3, where u_a , u_b and u_c are the modulating signals in the three-phase frame obtained by the inverse park transform of u_1 , u_2 . In addition, by using the HPWM SOC-balancing strategy, the switching functions for each of the H-bridge rectifiers can be obtained. The current commands in the d -axis and q -axis, i_{dref} and i_{qref} , are calculated from the active and reactive power commands, P_{ref} and Q_{ref} [3], as given by:

$$i_{dref} = 2P_{ref} / (3v_{sd}), \quad i_{qref} = 2Q_{ref} / (3v_{sd}) \quad (20)$$

It should be noted that the designed optimal controller in the d - q coordinates can also be applied to a single-phase CHB system by utilizing the single-phase d - q transformation, in which an imaginary phase M, lagging 90° from the real phase A, must be hypothesized [16].

B. DC-Link Voltage Controller for the IBDC

A set of stable and balanced dc-link voltages is a prerequisite for stable operation as well as high quality output ac waveforms of a PET-BESS, especially under a bidirectionally changed power flow and an uneven SOC of the submodule battery units. In this subsection, the control

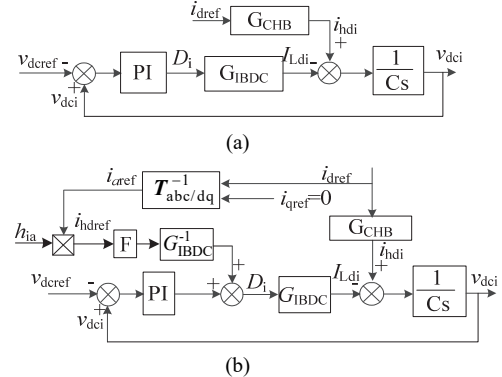


Fig. 4. Control diagram for the IBDC: (a) conventional one-loop control; (b) coordinative control with a feedforward loop.

design of the dc-link voltages for the IBDC is conducted.

According to Equation (6), the dependence of the dc-link voltage on the phase shift ratio of the IBDC can be illustrated as a first order differential equation. The conventional control schemes of the IBDC can be classified into two types: single loop voltage control [22] and voltage current double loop control [23]. Fig. 4(a) shows the diagram of the IBDC under voltage control, which is current sensorless. However, the power reference of the CHB frequently varies due to the application of a BESS, and it interferes in the stability control of the dc-link. The illustration mentioned above is described as an interference path in Fig. 4(a), in which G_{CHB} is the transfer function from the active current reference i_{dref} to the dc-link input current i_{hdci} .

In order to reduce the interference of the power reference on the dc-link voltage, a coordinative control strategy with the participation of the CHB signals is presented, as shown in Fig. 4(b), where the active current reference and switch status of the CHB form a feed-forward path to the dc-link voltage control.

In Fig. 4(b), i_{aref} denotes the sinusoidal current reference of the CHB in phase A, which can be obtained through the inverse park transform, $T_{abc/dq}^{-1}$, of i_{dref} and i_{qref} . G_{IBDC} is the transfer function from the phase shift ratio D_i to the input dc current i_{Ldi} of the IBDC, which can be determined according to (6).

$$G_{IBDC} = \frac{i_{Ldi}}{D_i} = \frac{n_t v_{bi}}{2 f_s L_t} (1 - 2 |\overline{D_i}|) \quad (21)$$

where $\overline{D_i}$ is the mean value of the phase shift ratio.

Being directly added to the phase shift ratio, as shown in Fig. 4(b), the feed-forward path introduces high frequency ripples to the dc-link voltage control. To avoid this disadvantage, a second-order low pass filter F is added to the feed-forward path to compensate for the high frequency component, and its transfer function is shown as follows:

$$F(s) = \frac{\omega_n^2}{s^2 + 2\xi\omega_n s + \omega_n^2} \quad (22)$$

Where ω_n and ζ are the natural frequency and damping ratio of the filter, respectively.

According to Fig. 4(a), the dc-link voltage PI controller can be designed by its compensated open loop transfer function, as expressed in (23).

$$G(s) = (k_{vp} + \frac{k_{vi}}{s}) \frac{G_{IBDC}}{Cs} \frac{1}{Ts+1} \quad (23)$$

Where, k_{vp} and k_{vi} are the proportion and integration constants of the voltage PI controller, and a low-pass function with a time constant T is added to represent the response delay of the dc current i_{Ldi} . The Bode diagram of (23) is shown in Fig. 5 with the parameters given in the simulation section. As shown in Fig. 5, the phase angle with a logarithmic magnitude of 0 dB is equal to -120.9° . Thus, the phase margin is $\phi_{pm}=180^\circ-120.9^\circ=59.1^\circ$. The logarithmic magnitude with a phase angle of -180° is negative infinity. Therefore, the gain margin is infinity. In addition, the damping ratio ξ_1 can be furtherly estimated as $\xi_1 \approx 0.01 \times \phi_{pm} = 0.59$ [24].

In the following, the damping effect on the dc-link voltage fluctuations of the conventional and the coordinative IBDC controller are analyzed. According to Fig. 4(a) and Fig. 4(b), the interference transfer functions of the conventional control and coordinative control with an input of i_{dref} and an output of dc-link voltage, can be derived as in (24) and (25).

$$G_{conv} = \frac{v_{dei}}{i_{dref}} = \frac{G_{CHB}(s)}{Cs + ((k_{vp} + k_{vi}/s))G_{IBDC}} \quad (24)$$

$$G_{coor} = \frac{v_{dei}}{i_{dref}} = \frac{G_{CHB}(s) - \frac{v_{sd}}{2Nv_{dc}}F(s)}{Cs + ((k_{vp} + k_{vi}/s))G_{IBDC}} \quad (25)$$

It should be noted that during the derivation of (25), the input-output power balance equation of the H-bridge rectifier is used, as shown in (26), where P_{aref} represents the power reference of the CHB rectifier in phase A, and N H-bridges are assumed to be power balanced.

$$P_{aref} = \frac{i_{dref}v_{sd}}{2} = Ni_{hdref}v_{dc} = Nh_{ia}i_{aref}v_{dc} \quad (26)$$

where v_{dc} is the average value of the dc-link voltages. The transfer function $G_{CHB}(s)$ in the interference path is determined by the grid current controller of the CHB. According to the grid current dynamic equation shown in (5) and the state-feedback control law shown in (19), the closed-loop transfer function of the active current of the CHB is obtained as:

$$\frac{i_d}{i_{dref}} = \frac{k_2s + k_1}{s^2 + k_2s + k_1} \quad (27)$$

Then the transfer function $G_{CHB}(s)$ can be expressed as:

$$G_{CHB}(s) = \frac{i_{hdri}}{i_{dref}} = \frac{i_{hdri}}{i_d} \frac{i_d}{i_{dref}} = \frac{1}{2} \frac{v_{sd}}{Nv_{dc}} \frac{k_2s + k_1}{s^2 + k_2s + k_1} \quad (28)$$

By substituting (21), (22) and (28) into (24) and (25), Bode plots of the interference transfer function of the two compared control methods for the IBDC are depicted in Fig.

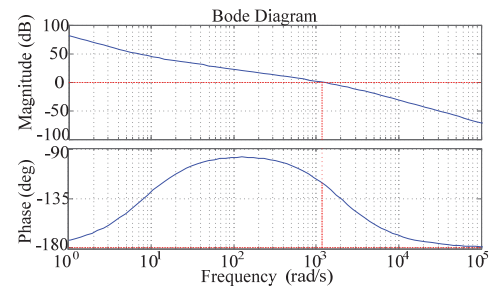


Fig. 5. Bode plots of the IBDC converter under voltage control.

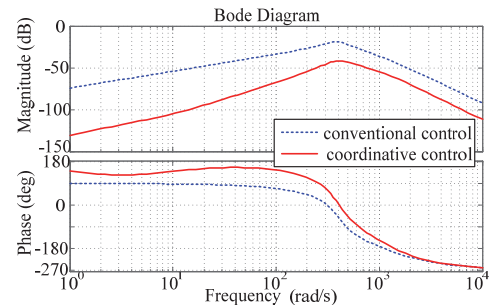


Fig. 6. Comparison of interference Bode plots between the coordinative control and the conventional control.

6. The parameters are given in the simulation section. As shown in Fig. 6, the interference gain of the proposed coordinative control is much smaller than that of the conventional control, which indicates that under the same power reference variations, the coordinative control can maintain the voltages on the dc-link with smaller fluctuations.

IV. HPWM BASED SOC BALANCING STRATEGY

By considering the manufacturing tolerances and unequal converter cell losses, etc., the SOC imbalance problem among the submodules cannot be neglected even when the battey voltages do not need to be controled. In this paper, the SOC balancing function is assigned to the front CHB by incorporating the battery SOC information into the HPWM modulation algorithm of the CHB.

The original study of the HPWM method for a CHB rectifier was done by M. Moosavi, H. Iman-Eini, et al. in [25]. This method aimed at balancing the dc-link voltages and obtaining reduced switching losses and a low THD. In this paper, the HPWM method is utilized to adjust the battery SOC to converge, in addition to its merits of a reduced switching frequency and a low THD.

The principle of the HPWM-based SOC-balancing method is illustrated in Fig. 7, where $h_1 \sim h_N$ are the switch functions for each H-bridge in a sequence with the corresponding battery SOC values arranged in ascending order. According to Fig. 7, when $u_a > 0$ and $i_a > 0$, the battery units with a lower SOC will be charged as the corresponding switch functions equal 1 (or a charging PWM), while the units with a higher SOC will be discharged as the corresponding switch

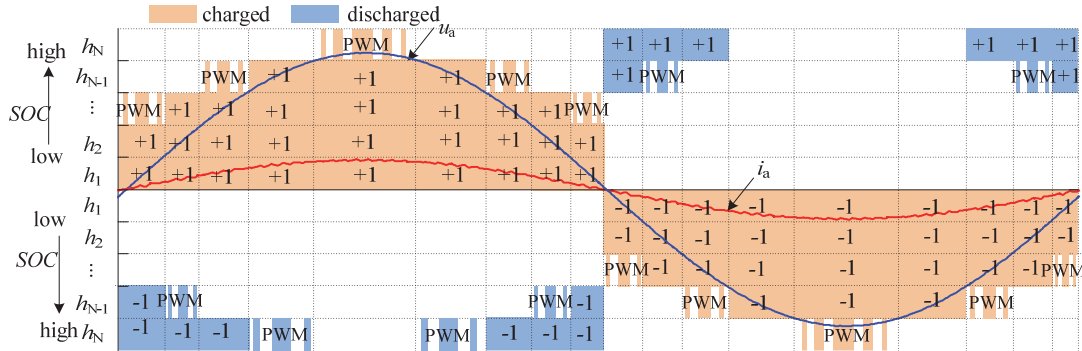


Fig. 7 Principle of the HPWM modulating strategy based on SOC sorting.

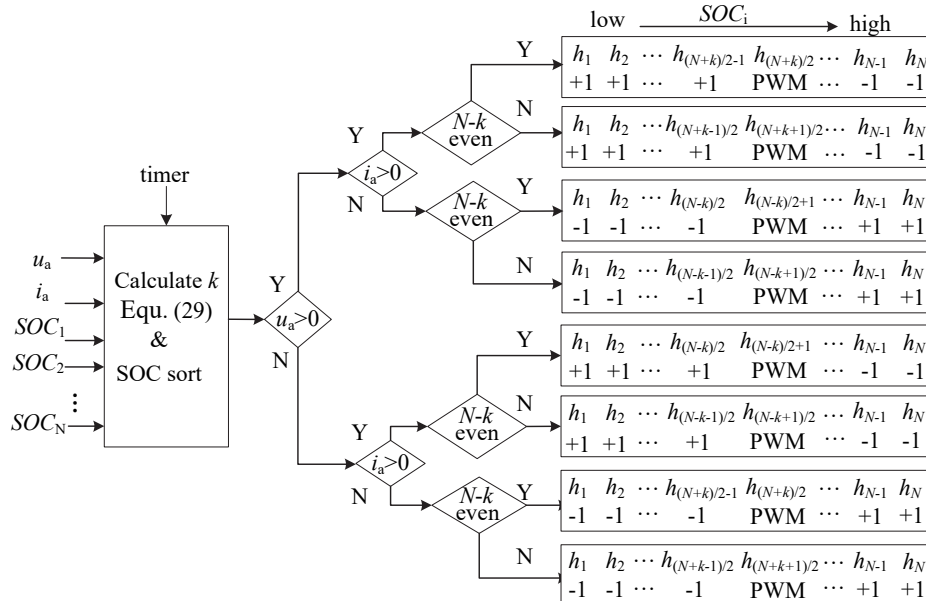


Fig. 8 Flowchart of the HPWM-SOC balancing algorithm.

functions equal -1 (or a discharging PWM). Actually, for each H-bridge unit, when $i_a > 0$, $h_i = 1$ means a positive output voltage and charging power into the battery unit; while $h_i = -1$ means a negative voltage and a discharge process. On the other hand, when $i_a < 0$, $h_i = 1$ means discharging, while $h_i = -1$ means charging. It is the different power flows among the submodules that drives the SOC for all of the battery units to converge and balance.

Therefore, according to Fig. 7, a flowchart of the rules based on the voltage region variable k and the SOC sorting of the battery-units are presented in Fig. 8 to carry out the switch functions for each of the H-bridges [25].

The voltage region k is defined as follows:

$$k = \text{floor}(|u_a|) + 1, \quad k = 1, 2, \dots, N \quad (29)$$

where the function $\text{floor}(\cdot)$ represents rounding the calculation to the nearest integer towards zero.

The modulating signal of the H bridge that works in the PWM mode is calculated as:

$$u_t = u_a - (k - 1)\text{sign}(u_a) \quad (30)$$

V. SIMULATION AND EXPERIMENTAL VERIFICATION

A. Simulation Results

A simulation model based on Fig. 1 has been built in MATLAB/Simulink to validate the proposed control strategy. The PET-BESS model consists of five H-bridge-IBDC units per phase. Each unit has a rated power of 166 kW (240kW peak), a total power of 2.5 MW, and a line-to-neutral voltage of 10 kV^{rms}. This configuration can be easily extended to medium voltage systems with ratings of 35 kV (line-to-line) and 5MW, which are usually used for integrating megawatt-scale PV or wind power plants [6]. All of the parameters of the system and circuits are listed in Table I. It should be noted that small capacity battery models of 300V/28A·h (not realistic) are chosen for the simulation in this paper to obtain an observable charge or discharge process in a short simulation time. However, in practical applications, a battery pack with a large capacity should be utilized (e.g., 300V, 2000Ah).

TABLE I
SIMULATION PARAMETERS FOR THE PET-BESS

Parameter	Symbol	Value
Line-to-neutral rms voltage	v_{sabc}	10 kV
Total power rating	P_{ref}	2.5 MW
Nominal dc-link voltage	v_{dcref}	3000 V
Input filter inductance	L_s	8 mH
Dc-link capacitor	C_i	20 mF
Leakage inductance of IBDC	L_t	0.152mH
Turn ratio of HF transformer	n_t	10
CHB' PWM carrier frequency	f_c	2 kHz
Switching frequency of IBDC	f_s	5 kHz
Battery nominal voltage		300 V
Battery nominal capacity		28 Ah

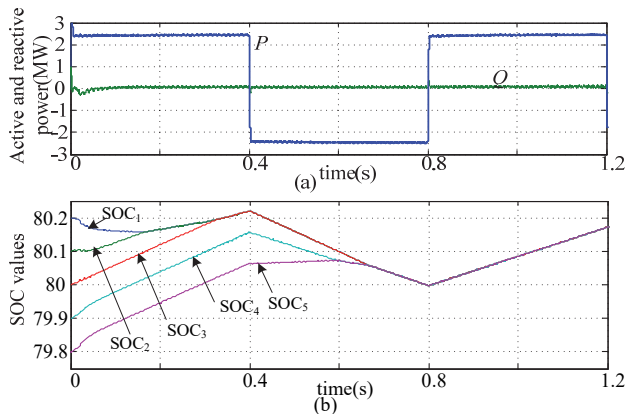


Fig. 9. Simulation waveforms of: (a) the three-phase active power P and reactive power Q ; (b) the SOC curves of the submodule battery units in phase A.

By using MATLAB instruction $K=lqr(A, B, Q, R)$, the feedback gains for the CHB controller can be obtained as $k_1=559$, $k_2=560$, $k_3=559$ and $k_4=560$. With these control parameters, the bandwidth of the CHB current controller is about 800 rad/s. The second-order filter F in the feed-forward path is chosen to have the same bandwidth as that of the CHB. Under this condition, the natural frequency and damping ratio of the filter can be set as $\omega_n=1200$, $\zeta=1$. The proportion and integration constants of the IBDC PI controller are $k_{vp}=0.0081$ and $k_{vi}=0.0652$, respectively.

The simulation condition is given as follows: the bidirectional active power reference P_{ref} varies between 2.5MW and -2.5MW, with a period of 0.8s, while Q_{ref} is set as 0VA for a unity power factor. The initial battery-unit SOC values are set as 80.2%, 80.1%, 80%, 79.9% and 79.8% to validate the HPWM based SOC balancing strategy.

Simulation waveforms of the three-phase active and reactive power as well as the submodule battery SOC curves in phase A are demonstrated in Fig. 9. These results confirm that the active and reactive power track the power commands well with a high dynamic performance. They also show that during the charge and discharge processes, the submodule battery SOC values converge effectively.

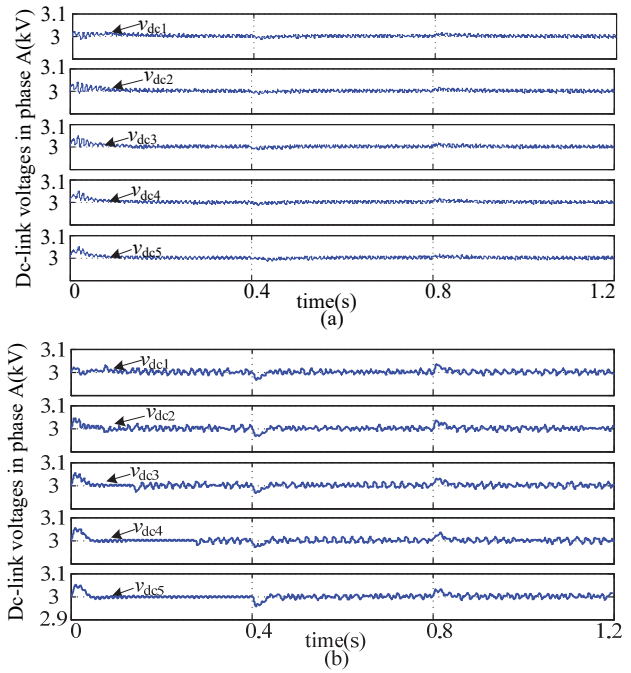


Fig. 10. Waveform comparison of the dc-link voltages in phase A, v_{dc1} - v_{dc5} , under: (a) the proposed coordinative control for the IBDC; (b) the conventional control for the IBDC.

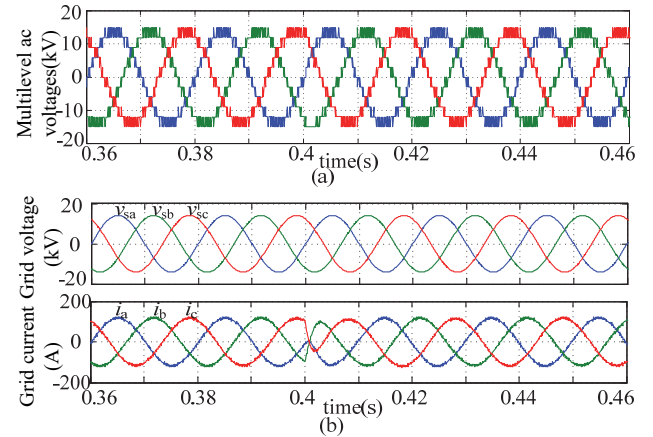


Fig. 11. Detailed waveforms of: (a) the three-phase multilevel ac voltages; (b) the three-phase grid voltages and grid currents.

Fig. 10 shows a comparison of the dc-link voltage responses between the proposed coordinative control and the conventional control for the IBDC. As can be seen, when the power reversed at 0.4s and 0.8s, there are significant drops and rises on the dc-link voltages under the conventional control. While under the proposed control the voltage drops and rises are much smaller.

Fig. 11 (a) shows the three-phase eleven-level ac output voltages of the CHB. They do not change obviously at 0.4s when the active power reversed, due to the high control performance of the dc-link voltages. The three-phase voltages and currents of the grid are shown in Fig.11 (b), which are in phase before 0.4s and out of phase after 0.4s under the

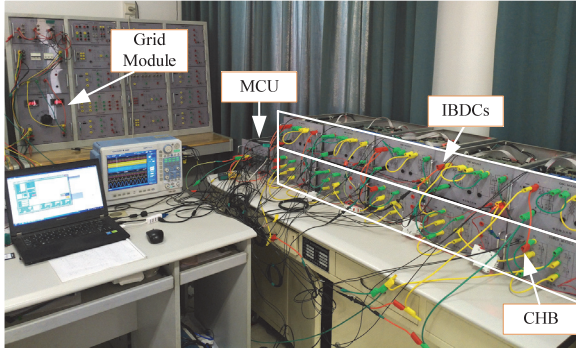


Fig. 12. Experimental setup of a single phase PET-BESS.

condition of $Q_{ref}=0$. In addition, the dynamic process of the grid current takes less than one line cycle, which demonstrates the good performance of the proposed state-feedback CHB controller.

B. Experimental Results

The proposed control method is validated on a laboratory scale prototype with one phase leg, as shown in Fig. 12. The prototype consists of one main controller unit (MCU), a CHB converter and five IBDCs. The grid voltage is 200V^{rms} (50 Hz), the rated power is 2kW, the utilized battery cells are of the Valve Regulated Lead Acid (VRLA) 60V/28A·h type, the dc-link capacitors are 4700 μ F, the dc-link voltage reference is 60V, and the turn ratio of the IBDC HF transformer is 1:1. The other parameters are the same as those in Table I.

In the MCU and in each of the submodules, a TMS320F28335 DSP is applied for the validation of the proposed control algorithm, and a Xilinx XC3S400 FPGA chip is responsible for processing the communication tasks and/or generating the firing pulses. All of the control signals are transmitted via optical fibers between the MCU and the CHB or IBDC submodules. As mentioned in section 4, the SOC sorting for multiple battery units is used in the HPWM method. Unfortunately, due to the absence of a battery energy management system (BEMS) in the lab at present, the SOC values are not available. As an alternative, to validate the HPWM based battery balancing strategy, sorting of the terminal voltages of the batteries is used to approximate the sorting of the SOC.

Firstly, experiment waveforms of the PET-BESS, including the dc-link and battery voltage v_{dcl} and v_{b1} , grid voltage v_{sa} , grid current i_a , and synthesized multilevel ac voltage v_{an} (defined in Equation (1)), are provided in Fig. 13(a). Corresponding results of a single-stage CHB-BESS are also given for comparison, which is shown in Fig. 13(b). During the experiment, the active power command P_{ref} is step changed from 800W to -800W.

As can be seen, in the PET-BESS, the dc-link voltage v_{dcl} can be effectively controlled to be constant when the active power is reversed and the battery terminal voltage v_{b1} is dropped. The steady state waveform of i_a is sinusoidal and

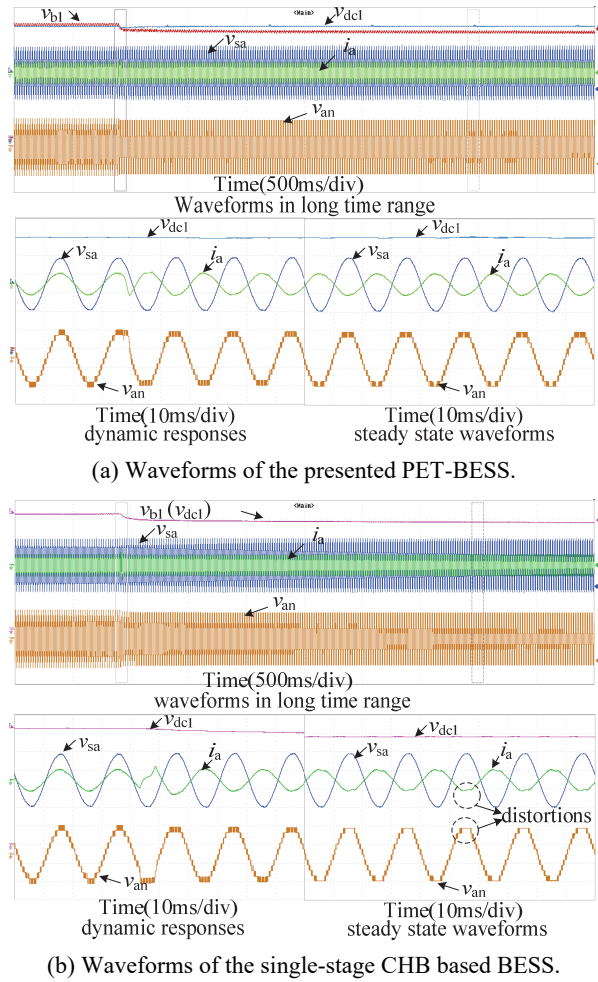


Fig. 13. Comparison waveforms of the BESS with and without the IBDC, including the grid voltage and the multilevel ac voltage, v_{sa} and v_{an} (200V/div), the grid current i_a (10A/div), and the dc-link and battery voltages v_{dcl} and v_{b1} (10V/div).

undistorted, and the multilevel ac voltage v_{an} is of good quality. Due to the well-designed CHB controller, the dynamic process of the grid current takes less than 0.02s. However, in the single-stage CHB-BESS, the dc-link voltage (which is equal to the battery voltage) drops about 5V (8.3%) after a power reversion due to the internal resistance of the battery. The voltage drop leads to over-modulation of the CHB, which causes distortions of the steady state waveforms of v_{an} and i_a .

Fig. 14 gives the ac terminal voltages for each of the H-bridge rectifiers and the synthesized eleven-level voltage, under the condition of a positive active power. As can be observed, the first, third and fifth H-bridges operate in the charge mode, since there are only unipolar switching modes in a half grid cycle for the three H-bridges. Meanwhile, there are both positive and negative (combining with PWM) switching modes in a half grid cycle for the second and fourth H-bridges, which work alternately in the charge and discharge process. These results are in accordance with the HPWM algorithm in Section IV.

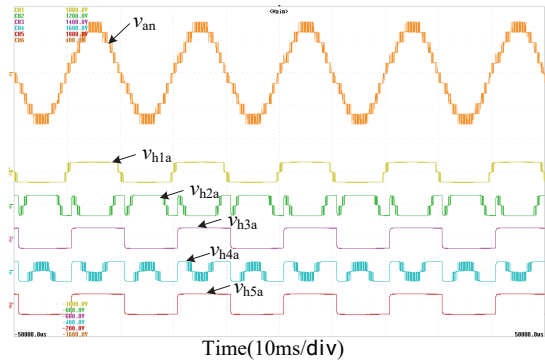
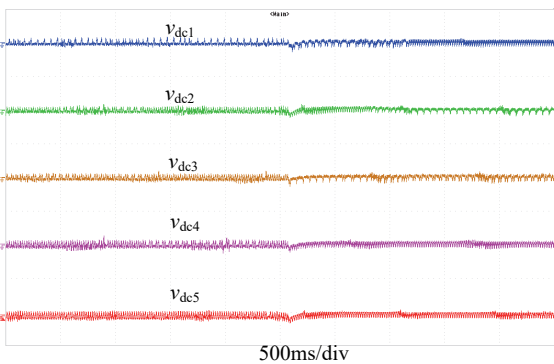
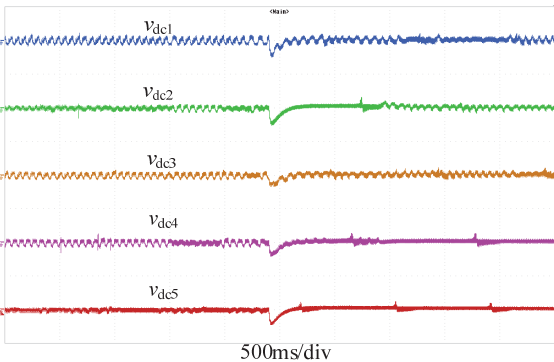


Fig. 14. AC terminal voltage for each of the H-bridges, v_{h1a} ~ v_{h5a} (200V/div), and the synthesized multilevel ac voltage v_{an} (200V/div).



(a) Dc-link voltages under the coordinative IBDC controller.



(b) Dc-link voltages under the conventional IBDC controller.

Fig. 15. Dc-link voltages v_{dc1} ~ v_{dc5} (2V/div) with a 60V dc bias under the two control strategies for the IBDC.

Fig. 15 shows a comparison of the dc-link voltage responses between the proposed coordinative control and the conventional control for the IBDC to a step change in the active power reference (800W to -800W). As can be seen, the dc-link voltage drops are much smaller when the coordinative scheme is used, and the dynamic process is faster.

Fig. 16 shows voltage and current waveforms of the IBDC in the bidirectional power flow cases. v_{dc1} and v_{b1} are the dc-link and battery terminal voltages. v_{pri} and v_{sec} are the ac voltages on the primary side and secondary side of the transformer. i_{L1} is the inductive current. As can be seen, with

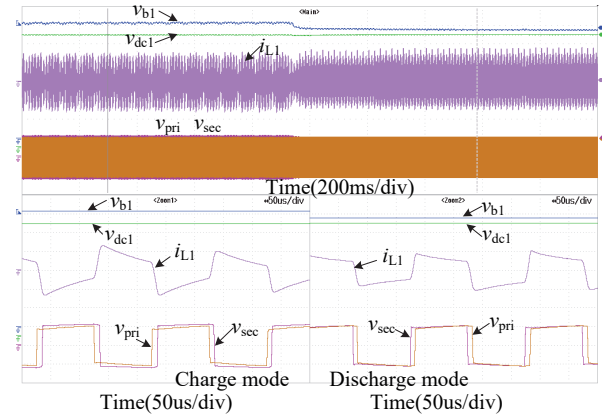


Fig. 16. Waveforms of the IBDC variables, including the input and output dc voltages of the IBDC, v_{dc1} and v_{b1} (10V/div), the inductive ac current i_{L1} (5A/div), and the primary and secondary side ac voltages, v_{pri} and v_{sec} (50V/div).

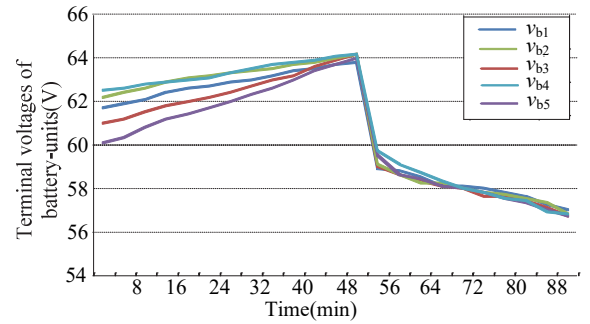


Fig. 17. Variation in the terminal voltages of five battery-units.

IBDC controlling, the dc-link voltage can maintain a constant value of 60V, when the power is reversed and a voltage drop appears on the battery terminal voltage. In the charge mode, the square wave voltage of the primary side leads the square wave voltage of the secondary side by a small phase angle. Meanwhile, in the discharge mode, the results are opposite. These results indicate that the IBDC circuits operate correctly.

Fig. 17 provides five convergent battery-unit terminal voltages, during a long-time charge and discharge process. The results confirm the validity of the HPWM-based battery balancing method. It should be noted that due to the internal impedance of the battery units, a voltage drop appears on all of the battery voltages when the power flow reversed.

VI. CONCLUSIONS

This paper presents a coordinative control strategy for a PET-BESS, which is based on the topology of the CHB and the IBDC. In the proposed method, the functions of power control and battery SOC balancing are assigned to the front CHB, while the dc-link voltages are controlled by the IBDC, with the power reference and switch status of the CHB taken as a feedforward. Better dynamic performances of the ac current, active power and reactive power can be achieved by

the state feedback and LQR methods for the CHB under a bidirectional power flow. The feedforward of the power reference and the switch status of the CHB effectively reduces the dc-link voltage fluctuations under power variations. With the battery SOC information incorporated into the HPWM modulation of the CHB, the SOC curves of the submodule battery-units converge effectively. Finally, simulations of a three-phase PET-BESS model and experiments on a single-phase scale-down prototype are conducted to confirm effectiveness of the presented control method.

ACKNOWLEDGMENT

This work was supported by the Fundamental Research Funds for the Central Universities under Grand No. 2017MS099, and the Independent Research Project of State Key Laboratory of Alternate Electrical Power System with Renewable Energy Sources (North China Electric Power University) under Grand No. LAPS2016-08.

REFERENCES

- [1] M. Sedghi, A. Ahmadian, E. Pashajavid, and M. Aliakbar-Golkar, "Storage scheduling for optimal energy management in active distribution network considering load, wind, and plug-in electric vehicles uncertainties," *J. Renew. Sustain. Energy*, Vol. 7, 033120, Jun. 2015.
- [2] M. S. Ballal, K. V. Bhadane, R. M. Moharil, and H. M. Suryawanshi, "A control and protection model for the distributed generation and energy storage system in microgrids," *Journal of Power Electronics*, Vol. 16, No. 2, pp. 748-759, Mar. 2016.
- [3] L. Maharjan, T. Yamagishi, and H. Akagi, "Active-power control of individual converter cells for a battery energy storage system based on a multilevel cascade PWM converter," *IEEE Trans. Power Electron.*, Vol. 27, No. 3, pp. 1099-1107, Mar. 2012.
- [4] W. Wang, F. Wu, K. Zhao, L. Sun, J. Duan, and D. Sun, "Elimination of the state-of-charge errors for distributed battery energy storage devices in islanded droop-controlled microgrids," *Journal of Power Electronics*, Vol. 15, No. 4, pp. 1105-1118, Jul. 2015.
- [5] K. F. Krommydas and A. T. Alexandridis, "Modular control design and stability analysis of isolated PV-source/battery-storage distributed generation systems," *IEEE Trans. Emerg. Sel. Topics Circuits Syst.*, Vol. 5, No. 3, pp. 372-382, Aug./Sep. 2015.
- [6] X. Yuan, "A set of multilevel modular medium-voltage high power converters for 10-MW wind turbines," *IEEE Trans. Sustainable Energy*, Vol. 5, No. 2, pp. 524-534, Apr. 2014.
- [7] Y. Zhuang, C. Wang, C. Wang, H. Cheng, Y. Gong, and H. Wang, "Determination method for topology configuration of hybrid cascaded H-bridge rectifiers," *Journal of Power Electronics*, Vol. 16, No. 5, pp. 1763-1772, Sep. 2016.
- [8] L. Maharjan, S. Inoue, and H. Akagi, "A transformerless energy storage system based on a cascade multilevel PWM converter with star configuration," *IEEE Trans. Ind. Appl.*, Vol. 44, No. 5, pp. 1621-1630, Sep./Oct. 2008.
- [9] D.-H. Shin, J.-B. Jeong, T.-H. Kim, and H.-J. Kim, "Modeling of lithium battery cells for plug-in hybrid vehicles," *Journal of Power Electronics*, Vol. 13, No. 3, pp. 429-436, May 2013.
- [10] I. Trintis, S. Munk-Nielsen, and R. Teodorescu, "Cascaded H-bridge with bidirectional boost converters for energy storage," in *Proceedings of the 2011 European Conference on Power Electronics and Applications (EPE)*, pp. 1-9, Aug. 2011.
- [11] H. Qin and J. W. Kimball, "Generalized average modeling of dual active bridge dc-dc converter," *IEEE Trans. Power Electronics*, Vol. 27, No. 4, pp. 2078-2084, Apr. 2012.
- [12] J. W. Kolar and G. Ortiz, "Solid-state-transformers: key components of future traction and smart grid systems," in *Proceedings of the International Power Electronics Conference-ECCE Asia (IPEC 2014)*, May 2014.
- [13] B. Zhao, Q. Song, W. Liu, and Y. Sun, "Overview of dual-active bridge isolated bidirectional DC-DC converter for high-frequency-link power-conversion system," *IEEE Trans. Power Electron.*, Vol. 29, No. 8, pp. 4091-4106, Aug. 2014.
- [14] Z. Gao and H. Fan, "A modular bi-directional power electronic transformer," *Journal of Power Electronics*, Vol. 16, No. 2, pp. 399-413, Mar. 2016.
- [15] H. Iman-Eini, J.-L. Schanen, Sh. Farhangi, J. Barbaroux, and J.P. Keradec, "A power electronic based transformer for feeding sensitive loads," in *Proceedings of the 2008 IEEE Power Electronics Specialists Conference*, pp. 2549-2555, Jun 2008.
- [16] J. Shi, W. Gou, H. Yuan, T. Zhao, and A. Q. Huang, "Research on voltage and power balance control for cascaded modular solid-state transformer," *IEEE Trans. Power Electron.*, Vol. 26, No. 4, pp. 1154-1166, Apr. 2011.
- [17] T. Zhao, G. Wang, S. Bhattacharya, and A. Q. Huang, "Voltage and power balance control for a cascaded H-bridge converter-based solid-state transformer," *IEEE Trans. Power Electron.*, Vol. 28, No. 4, pp. 1523-1532, Apr. 2013.
- [18] B. Zhao, Q. Song, W. Liu, and Y. Sun, "A synthetic discrete design methodology of high-frequency isolated bidirectional DC/DC converter for grid-connected battery energy storage system using advanced components," *IEEE Trans. Ind. Electron.*, Vol. 61, No. 10, pp. 5402-5410, Oct. 2014.
- [19] Q. Miao, J. Wu, H. Ai, J. Y. Wu, H. K. Ai, F. Xiong, D. W. Qi, and L. L. Hao, "Study on coordinating control strategy of hybrid cascade energy storage and bi-directional power regulation device," *Advanced Materials Research*, Vol. 852, pp. 655-659, Jan. 2014.
- [20] M. Ornik and M. E. Broucke, "A topological obstruction to reach control by continuous state feedback," in *IEEE Annual Conference on Decision and Control (CDC)*, pp. 2258-2263, Dec. 2015.
- [21] D. Shuai, Y. Xie, and X. Wang, "Optimal control of buck converter by state feedback linearization," in *Proceedings of the 7th World Congress on Intelligent Control and Automation*, pp. 2265-2270, Jun. 2008.
- [22] D. Segaran and D. G. Holmes, "Enhanced load step response for a bidirectional DC-DC converter," *IEEE Trans. Power Electron.*, Vol. 28, No. 1, pp. 371-379, Jan. 2013.
- [23] Y. Tian, Z. Chen, F. Deng, X. Sun, and Y. Hu, "Active power and DC voltage coordinative control for cascaded DC-AC converter with bidirectional power application," *IEEE Trans. Power Electron.*, Vol. 30, No. 10, pp. 5911-5925, Oct. 2015.
- [24] R. C. Dorf and R. H. Bishop, *Modern Control Systems*. 12th

- ed., Pearson Education Group, Chapter 9, pp. 653-660, 2013.
- [25] M. Moosavi, G. Farivar, H. Iman-Eini, and S. M. Shekarabi, "A voltage balancing strategy with extended operating region for cascaded H-bridge converters," *IEEE Trans. Power Electron.*, Vol. 29, No. 9, pp. 5044-5053, Sep. 2014.



Yuwei Sun was born in Tangshan, China, in 1987. She received her M.S. degree in Power Electronics from the North China Electric Power University, Baoding, China, in 2013. She is presently working toward her Ph.D. degree in Electrical Engineering from the North China Electric Power University, Beijing, China. Her current research interests include power electronics technology applications in power systems, and power electronic transformers.



Jiaomin Liu received his B.S. degree in Automation, and his Ph.D. degree from the Hebei University of Technology, Tianjin, China, in 1982 and 1998, respectively. He is presently working as a Professor in the School of Electrical and Electronics Engineering at the North China Electric Power University, Beijing, China. His current research interests include new energy power system characteristics and supplemental multi-power sources.



Yonggang Li received his M.S. and Ph.D. degrees in Electrical Engineering from the North China Electric Power University, Beijing, China, in 1995 and 1999, respectively. He is presently working as a Professor in the School of Electrical and Electronics Engineering at the North China Electric Power University. His current research interests include power system operation analysis, renewable energy and electric equipment.



Chao Fu received his M.S. and Ph.D. degrees in Electrical Engineering from the North China Electric Power University, Beijing, China, in 2006 and 2012, respectively. He is presently working as a Lecturer in the School of Electrical and Electronics Engineering at the North China Electric Power University, Baoding, China. His current research interests include renewable energy generation and power electronics technology applications in power systems.



Yi Wang received his B.S. and Ph.D. degrees in Electrical Engineering from the North China Electric Power University, Beijing, China, in 1999 and 2005, respectively. He is presently working as a Professor in the School of Electrical and Electronics Engineering at the North China Electric Power University. His current research interests include power electronics applications in power systems, wind power integration, VSC-HVDC, and dc grids.